Supporting Information for "High-speed and Low-energy Actuation for Pneumatic Soft Robots with Internal Exhaust Air Recirculation"

Miao Feng[1,2], Dezhi Yang[1,2], Carmel Majidi[3,4], and Guoying Gu[1,2,5]

[1]Robotics Institute, School of Mechanical Engineering, Shanghai Jiao Tong University, Shanghai, 200240, China.
[2]State Key Laboratory of Mechanical System and Vibration, Shanghai Jiao Tong University, Shanghai, 200240, China.
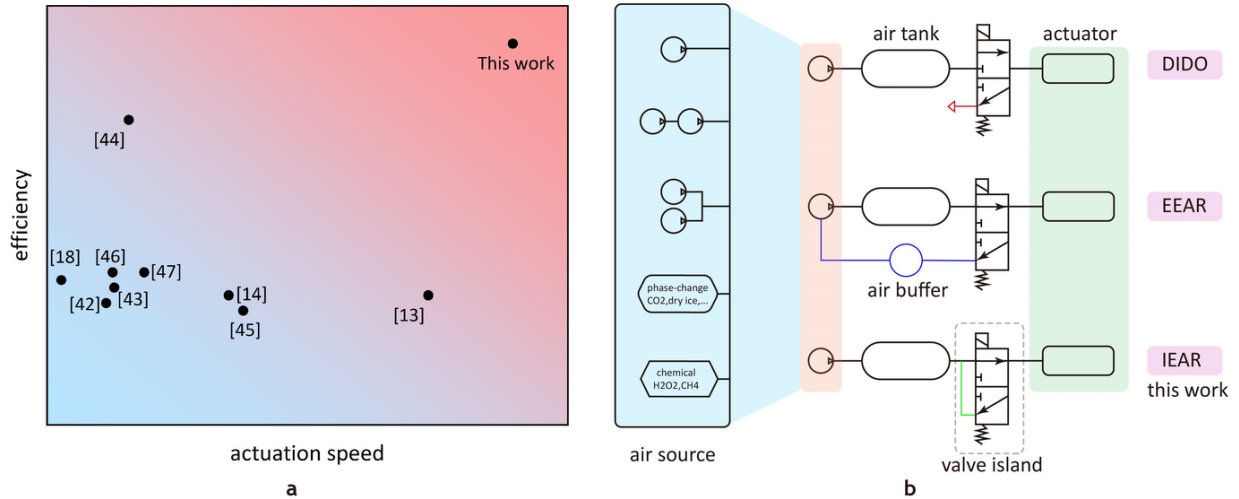[3]Carnegie Mellon University
[4]Soft Machines Lab, Carnegie Mellon University, Pittsburgh, PA 15213, USA.
[5]Meta Robotics Institute, Shanghai Jiao Tong University, Shanghai, 200240, China.

September 27, 2022

Table S1.   Performance of soft pneumatic actuators

Supplementary Figures

Figure S1. Performance of typical soft pneumatic actuators and typical air supply systems. a The actuation speed and efficiency of typical pneumatic soft actuators. The actuation speed and the efficiency depend on the pressure of the air source, working pressure, actuator, and actuation mechanism, which makes it challenging to compare actuation speed and efficiency with the same scale. Here, we present

a normalized indicator $\frac{p_{work}Vf}{p_{source}}$ as a metric for actuation speed based on **Table S1**. And the efficiency is qualitative according to existing research.[22,34,43,44] **b** Typical air supply systems. The air source includes single, serial, parallel pumps, and air source with phase-change medium and chemical pumps. The supplying mechanisms include DIDO, EEAR, and IEAR (this work). These air source and supplying mechanisms can be further combined to achieve various performances.[34,43,44,48,49]
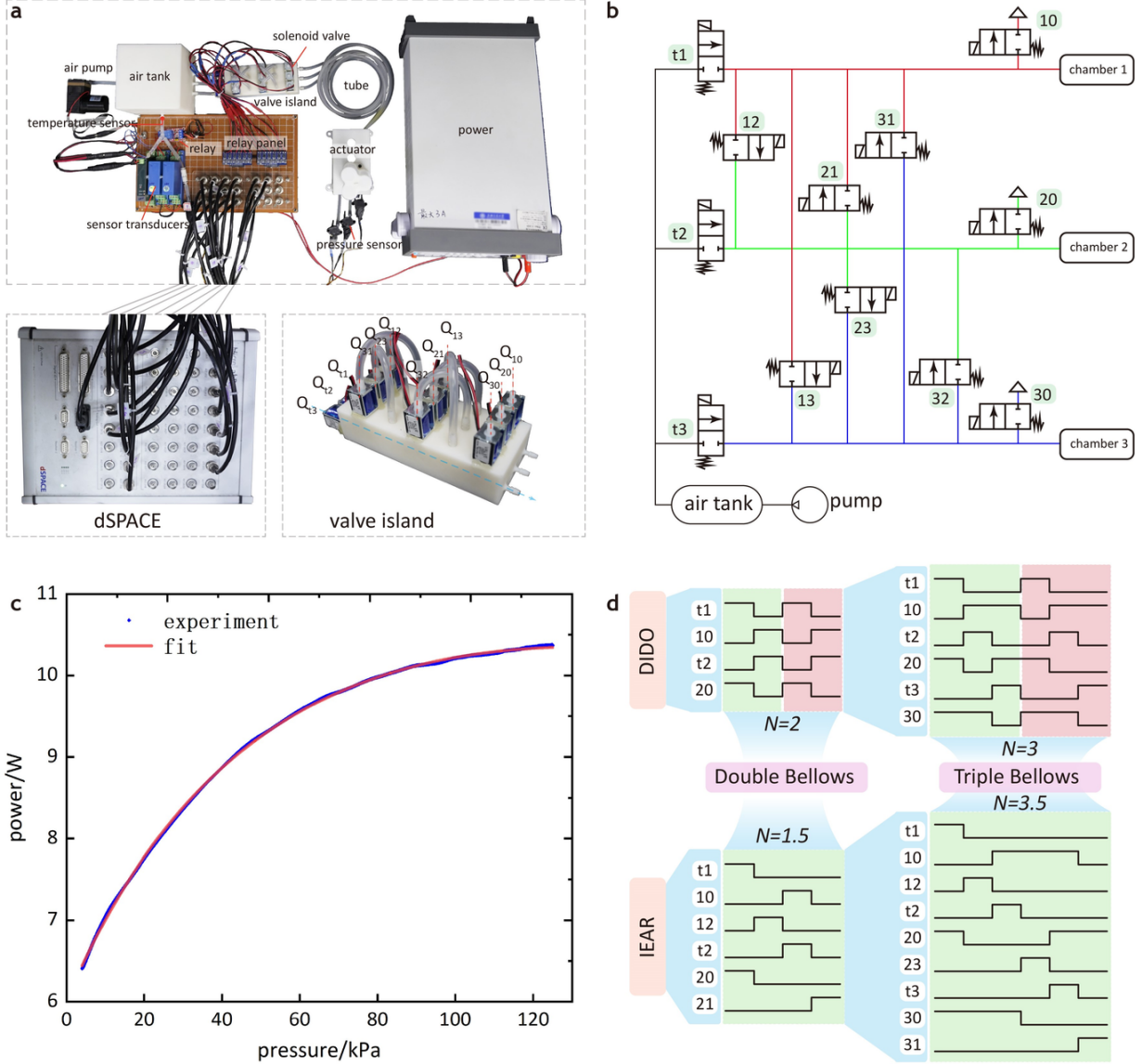
Figure S2. The experimental setup and platform. a The overview of the experimental sets. The DSPACE controls the system (1 kHz), and the 3-channel valve island produces the timings of valves. **b** Pneumatic schematic diagram of the 3-channel valve island. **c** Power function of the air pump, where the pump power increases with the output pressure. **d** Timings of the solenoid valves. N is the time-based equivalent weighted average number of solenoid valves in use for a period, which is obtained from the timings.

2
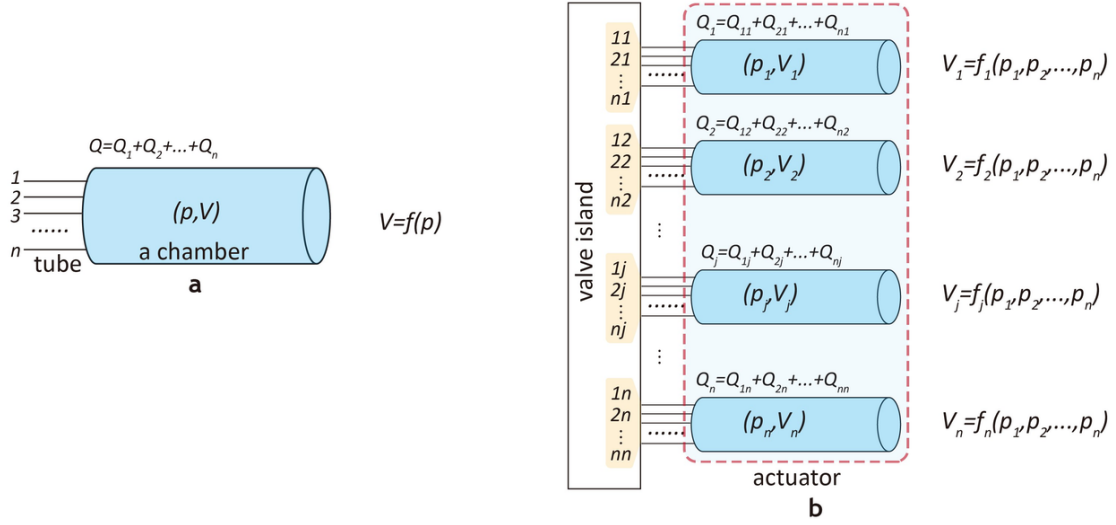
Figure S3. Dynamic modeling of m-SPAs. a Actuator with a single chamber having n inlet tubes. **b** m-SPAs with n chambers, and each chamber connects to other chambers with n inlet tubes. The chambers of m-SPAs can exchange pressurized air and influence the motion of each other.
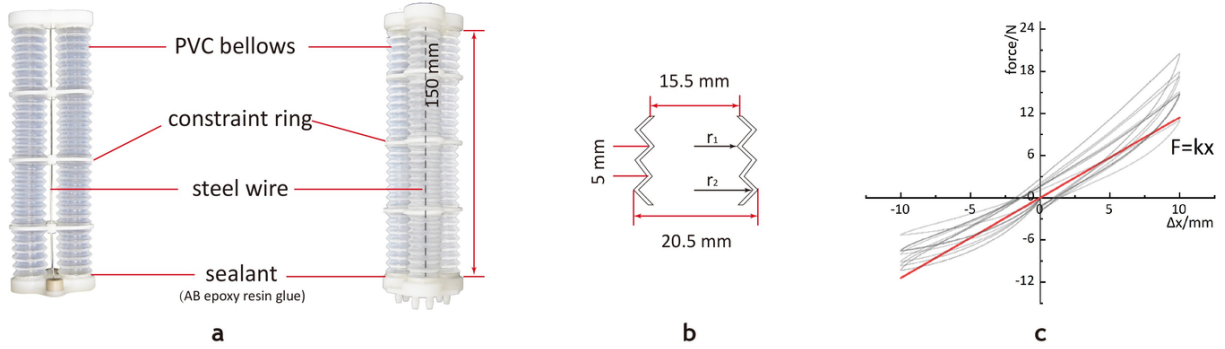
Figure S4. The materials, geometry, and stiffness of the business PVC bellows. a Detailed structure of the exemplary actuators. **b** Geometry parameters of the extensible commercial bellows-shaped PVC tube. **c** Stiffness curve of the PVC tube, obtained from seven tubes with a relaxed length of 50 mm. This work uses the PVC tube as a structure with linear elasticity.

3
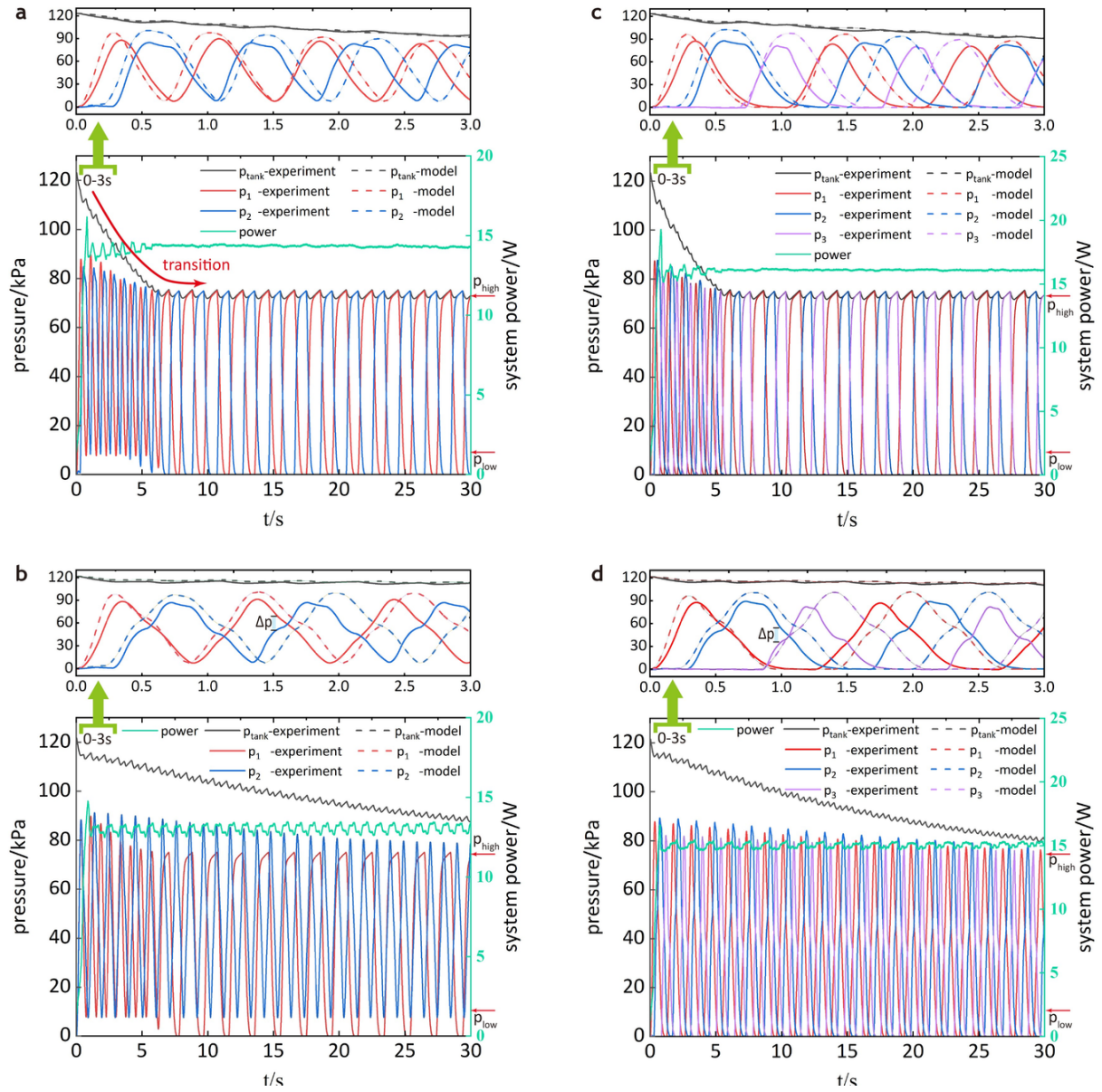
Figure S5. Theoretical and experimental pressures of Double Bellows and Triple Bellows (0-30 s and detailed 0-3 s). a Pressures of the Double Bellows with DIDO. Following the initial actuation cycles, the Double Bellows exhibits a rapid transition and enters a steady-state pressure response. **b** Pressures of the Double Bellows with IEAR. A more gentle transition means enhanced air supply ability. **c** Pressures of the Triple Bellows with DIDO. **d** Pressures of Tripe Bellows with IEAR. The discrepancy between the model and experiments, especially the cumulative time shift, might come from the ignorance of the actuator mass, actuator volume modeling error, and inconsistency of the used commercial solenoid valves.

4
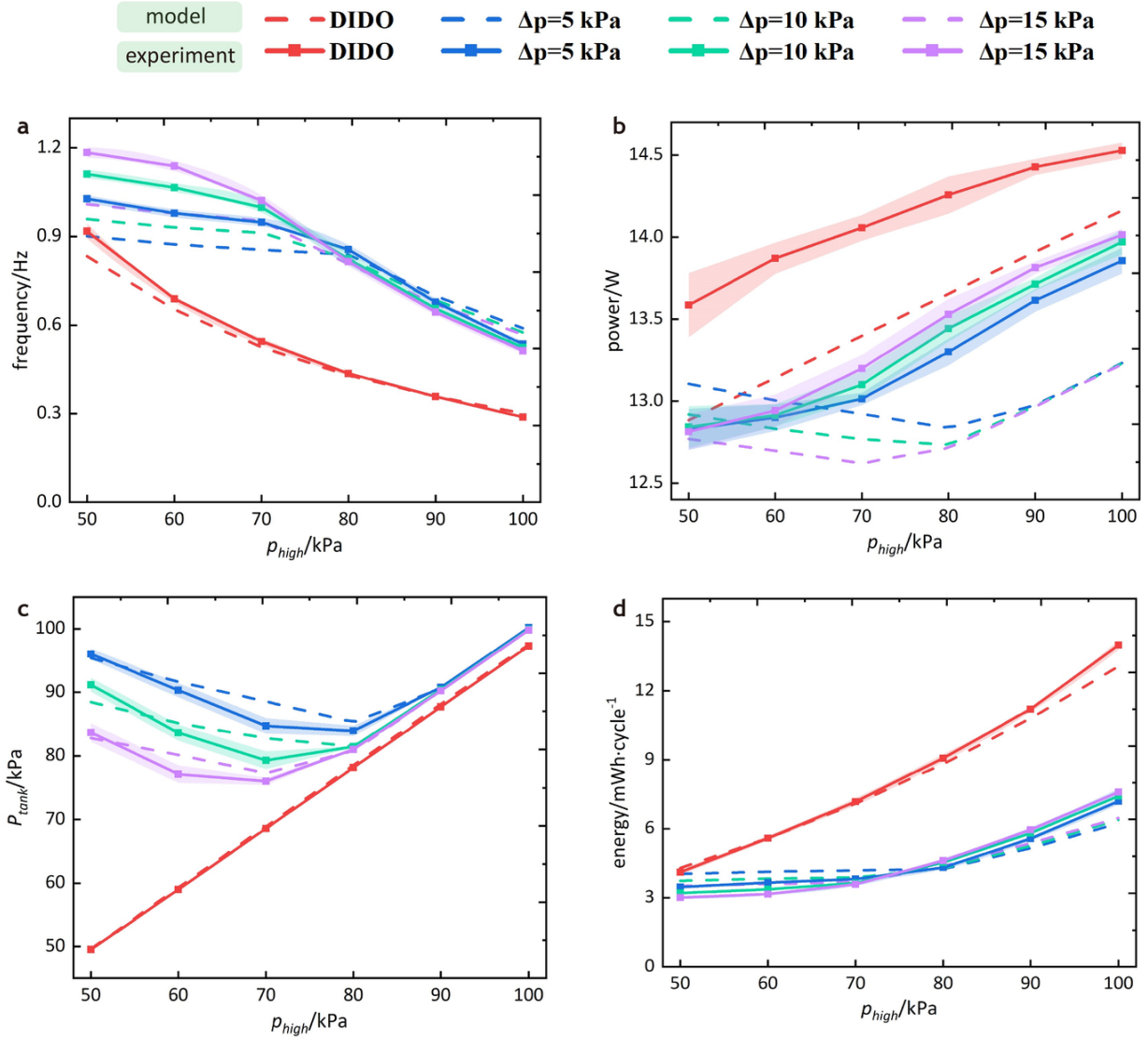
Figure S6. Influence of Δp on actuation performance of the Double Bellows. The experiments include DIDO and IEAR with Δp =5, 10, 15 kPa and p_{low} =10 kPa. **a** Steady-state actuation frequency. **b** Steady-state system power. **c** Steady-state supplied air pressure (p_{tank}). **d** Steady-state energy consumption per cycle. The model can predict the actuation performance with some errors (**Supplementary Note 1**).

Figure S7. Influence of Δp on actuation performance of the Triple Bellows. The experiments include DIDO and IEAR with $\Delta p =$5, 10, 15 kPa and $p_{low} =$10 kPa. **a** Steady-state actuation frequency. **b** Steady-state system power. **c** Steady-state supplied air pressure (p_{tank}). **d** Steady-state energy consumption per cycle. The model can predict the actuation performance with some errors (**Supplementary Note 1**).
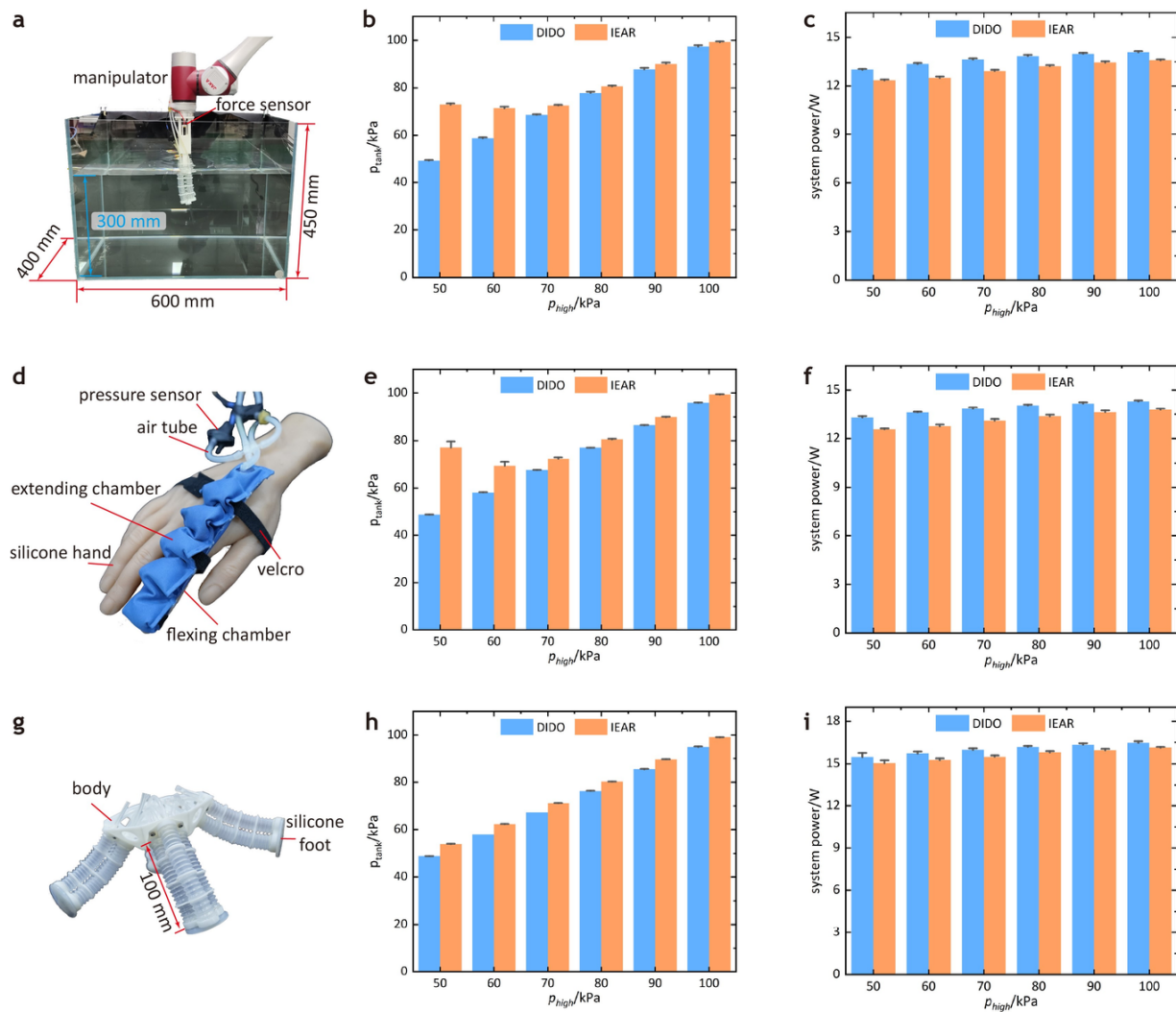
Figure S8. The detailed components of the soft robotic applications and their performances of supplied pressure and system power. a system overview of the robotic fin fixed on a manipulator. **b** air tank pressure p_{tank} when supplying the robotic fin. **c** System power when actuating the robotic fin. **d** Components employed in the fabric-based actuator application. **e** Supplied air pressure p_{tank} when supplying the fabric-based actuator. **f** System power when actuating the fabric-based actuator. **g** Composition of the quadruped robot. **h** Supplied air pressure p_{tank} when supplying the quadruped robot. **i** System power when actuating the quadruped robot.
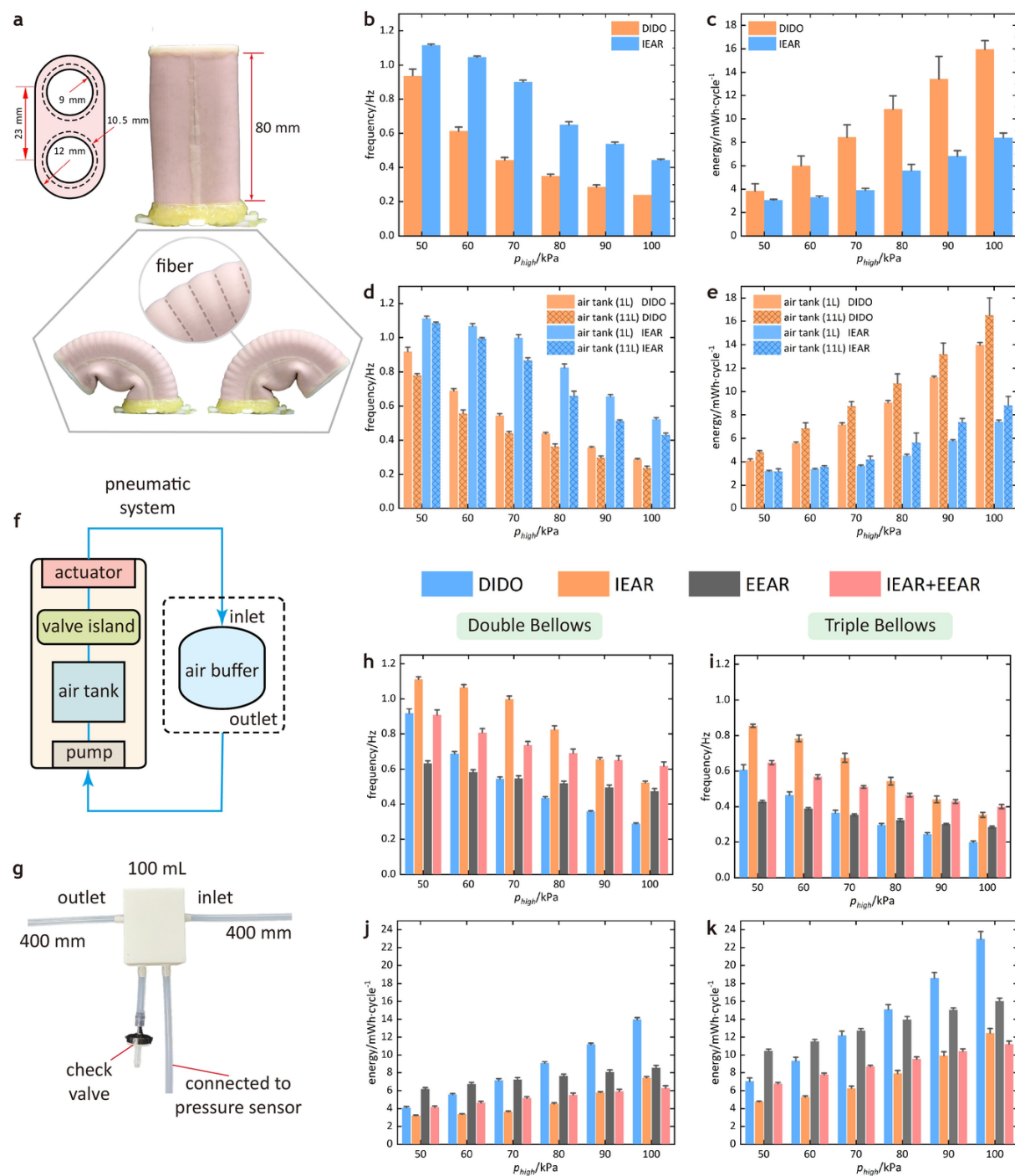
Figure S9. Application on a silicone actuator, the influence of a larger air tank on IEAR, and the comparison with EEAR. a Fiber-reinforced silicone actuator with two chambers. **b** Actuation frequency of the silicone actuator with DIDO and IEAR. **c** Energy consumption per cycle of the silicone actuator with DIDO and IEAR. **d** Actuation frequency of Double Bellows with the air tank volume 1 L and 11L, respectively. **e** Energy consumption per cycle of Double Bellows with the air tank volume 1 L

8

and 11L, respectively. **f** System configuration of EEAR, where the air buffer is introduced to recycle the exhaust air. **g** The structure of the 100 mL air buffer. **h** Actuation frequency of Double Bellows with four modes: DIDO, IEAR, EEAR, and DIDO+EEAR. **i** Actuation frequency of Triple Bellows with four modes as before. **j** Steady-state actuation frequency of Double Bellows with four modes as before. **k** Steady-state actuation frequency of Triple Bellows with four modes as before.
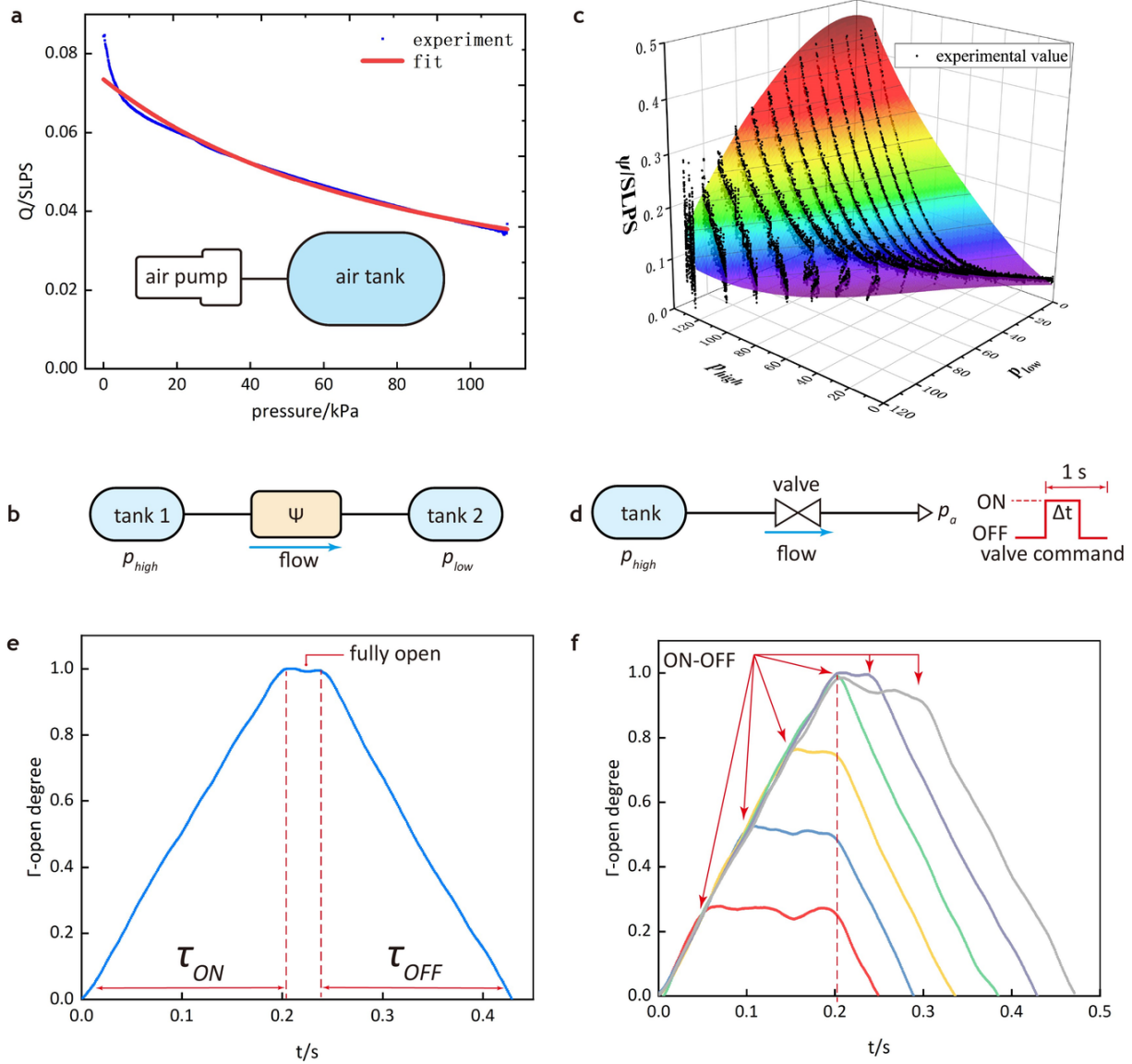
Figure S10. Calculation, characterization, and correction of mass flow. a Flow characteristics of air pump and the schematic diagram of the measurement method. (**Supplementary Note 10**) **b** The component is inserted between two air tanks to characterize the flow function of the corresponding air passage. (**Supplementary Note 11**) **c** Flow function of corresponding air passage (the results in the graph are ψ_{t1}). **d** Characterization method of the valve switch characteristics. **e** Opening and closing characteristics of solenoid valves. **f** Experimentally obtained open degree when ON-OFF command change occurs at $\Delta t = 0.05, 0.10, 0.15, 0.20,$ and 0.25 s. (**Supplementary Note 12**)

9

Supplementary Notes

Supplementary Note 1. Detailed modeling of m-SPAs

We develop the dynamic model with the following assumptions: i) the air is an ideal gas; ii) the air temperature is constant; iii) the volume of each chamber is a function of internal pressures; iv) the pressure in each chamber is uniformly distributed; v) the mass of m-SPAs is ignored due to their lightweight, and the deformation of m-SPAs is a function of internal pressures.

We have defined $\xi = \frac{\rho RT}{M}$ in Formula (2). The detailed modeling of m-SPAs is as follows.

Note: All the following equations defined for the first time should have the index form (SX) . Due to the compilation error of the webpage, the following display might lack an "S". However, if you export a pdf version, the display is complete.

·Modeling of an actuator with a single chamber (**Figure S3a**).

The modeling is based on Clapeyron Equation (ideal gas equation).

$$pV = \eta RT \tag{S1}$$

We can obtain the differential form of the equation to time.

$$\dot{p}V + p\dot{V} = \xi Q \tag{S2}$$

Hypothesize that the chamber volume is the function of internal pressure.

$$V = f(p) \tag{S3}$$

$$\dot{V} = \frac{df}{dp}\dot{p} \tag{S4}$$

By substituting Equation (S4) into Equation (S2), we have the dynamic pressure of the actuator.

$$\dot{p} = \frac{\xi Q}{V + p\frac{df}{dp}} \tag{S5}$$

$$p = p' + p_a$$

The variables and parameters are defined as follows.

p-abosolute pressure
p'-gauge pressure
p_a-atmosphere pressure
V-instantaneous volume of a chamber
η-amount of melocules
R-ideal gas constant

T-absolute temperature

M-Molar mass of air

ρ-air density under the standard condition

Q-mass flow into a chamber

·Modeling of m-SPAs (**Figure S3b**).

We generalize Equation (S2) to an actuator with n chambers.

$$\dot{p}_1 V_1 + p_1 \dot{V}_1 = \xi Q_1 \tag{1}$$
$$\dot{p}_2 V_2 + p_2 \dot{V}_2 = \xi Q_2$$
$$\cdots\cdots$$
$$\dot{p}_j V_j + p_j \dot{V}_j = \xi Q_j$$
$$\cdots\cdots$$
$$\dot{p}_n V_n + p_n \dot{V}_n = \xi Q_n \tag{S6}$$

Where

$$V_1 = f_1 (p_1, p_2, \cdots, p_n)$$
$$V_2 = f_2 (p_1, p_2, \cdots, p_n)$$
$$\cdots\cdots$$
$$V_j = f_j (p_1, p_2, \cdots, p_n)$$
$$\cdots\cdots$$
$$V_n = f_n (p_1, p_2, \cdots, p_n) \tag{S7}$$

$$\dot{V}_1 = \frac{\partial f_1}{\partial p_1}\dot{p}_1 + \frac{\partial f_1}{\partial p_2}\dot{p}_2 + \cdots + \frac{\partial f_1}{\partial p_n}\dot{p}_n$$
$$\dot{V}_2 = \frac{\partial f_2}{\partial p_1}\dot{p}_1 + \frac{\partial f_2}{\partial p_2}\dot{p}_2 + \cdots + \frac{\partial f_2}{\partial p_n}\dot{p}_n$$
$$\cdots\cdots$$
$$\dot{V}_j = \frac{\partial f_j}{\partial p_1}\dot{p}_1 + \frac{\partial f_j}{\partial p_2}\dot{p}_2 + \cdots + \frac{\partial f_j}{\partial p_n}\dot{p}_n$$
$$\cdots\cdots$$
$$\dot{V}_n = \frac{\partial f_n}{\partial p_1}\dot{p}_1 + \frac{\partial f_n}{\partial p_2}\dot{p}_2 + \cdots + \frac{\partial f_n}{\partial p_n}\dot{p}_n \tag{S8}$$

The mass flow Q_j into the chamber j is the sum of flows from all other chambers.

$$Q_j = \sum_{i=1}^{n} Q_{ij} \tag{S9}$$

Where Q_{ij} is obtained from the data-driven flow function (4).

11

$$Q_{ij} = \Psi_{ij}\left(p_i, p_j\right) \; \left(p_i \geqslant p_j\right)$$

Combining Equation (S5)-(S8), we can rewrite Equation (S6) as

$$\begin{bmatrix} V_1 & & & \\ & V_2 & & \\ & & \ddots & \\ & & & V_n \end{bmatrix} \begin{bmatrix} \dot{p}_1 \\ \dot{p}_2 \\ \vdots \\ \dot{p}_n \end{bmatrix} + \begin{bmatrix} p_1 & & & \\ & p_2 & & \\ & & \ddots & \\ & & & p_n \end{bmatrix} \begin{bmatrix} \frac{\partial f_1}{\partial p_1} & \frac{\partial f_1}{\partial p_2} & \cdots & \frac{\partial f_1}{\partial p_n} \\ \frac{\partial f_2}{\partial p_1} & \frac{\partial f_2}{\partial p_2} & \cdots & \frac{\partial f_2}{\partial p_n} \\ \vdots & \vdots & \ddots & \vdots \\ \frac{\partial f_n}{\partial p_1} & \frac{\partial f_n}{\partial p_2} & \cdots & \frac{\partial f_n}{\partial p_n} \end{bmatrix} \begin{bmatrix} \dot{p}_1 \\ \dot{p}_2 \\ \vdots \\ \dot{p}_n \end{bmatrix} = \xi \begin{bmatrix} Q_1 \\ Q_2 \\ \vdots \\ Q_n \end{bmatrix} \qquad \text{(S10)}$$

Which can be further abbreviated as

$$diag\left(\boldsymbol{V}\right)\dot{\boldsymbol{p}} + diag\left(\boldsymbol{p}\right)\frac{\partial \boldsymbol{V}}{\partial \boldsymbol{p}}\dot{\boldsymbol{p}} = \xi\boldsymbol{Q} \qquad \text{(S11)}$$

So the dynamic pressure is dominated by Equation (1).

$$\dot{\boldsymbol{p}} = \xi\left[diag\left(\boldsymbol{V}\right) + diag\left(\boldsymbol{p}\right)\frac{\partial \boldsymbol{V}}{\partial \boldsymbol{p}}\right]^{-1}\boldsymbol{Q}$$

Where the Jacobian matrix of chamber volume is

$$\frac{\partial \boldsymbol{V}}{\partial \boldsymbol{p}} = \begin{bmatrix} \frac{\partial f_1}{\partial p_1} & \frac{\partial f_1}{\partial p_2} & \cdots & \frac{\partial f_1}{\partial p_n} \\ \frac{\partial f_2}{\partial p_1} & \frac{\partial f_2}{\partial p_2} & \cdots & \frac{\partial f_2}{\partial p_n} \\ \vdots & \vdots & \ddots & \vdots \\ \frac{\partial f_n}{\partial p_1} & \frac{\partial f_n}{\partial p_2} & \cdots & \frac{\partial f_n}{\partial p_n} \end{bmatrix} \qquad \text{(S12)}$$

For the definitions of these variables, please refer to "the dynamic model of m-SPAs" in the main text.

The above dynamic model of m-SPAs is generally important to these multi-chamber lightweight soft/rigid actuators, even if their chambers have mutual interactions. Notably, since we do not consider the mass, hysteresis, or creep of the actuator, the model inaccuracy might increase for these actuators with great mass or materials that are not elasticity-dominated.

Supplementary Note 2. Modeling of the Double Bellows

·Dynamic pressure of the Double Bellows

Here, the air tank in the Double Bellows $(i=1,2)$ is regarded as a chamber with a constant volume V_t. The chamber volume V_1 and V_2 are independent of V_t.

$$V_i = f_i\left(p_1, p_2\right)$$

We specify Equation (1) on the Double Bellows.

$$\dot{\boldsymbol{p}} = \begin{bmatrix} \dot{p}_1 \\ \dot{p}_2 \\ \dot{p}_t \end{bmatrix} \quad \boldsymbol{p} = \begin{bmatrix} p_1 \\ p_2 \\ p_t \end{bmatrix} \quad \boldsymbol{V} = \begin{bmatrix} V_1 \\ V_2 \\ V_t \end{bmatrix} \quad \frac{\partial \boldsymbol{V}}{\partial \boldsymbol{p}} = \begin{bmatrix} \frac{\partial f_1}{\partial p_1} & \frac{\partial f_1}{\partial p_2} & 0 \\ \frac{\partial f_2}{\partial p_1} & \frac{\partial f_2}{\partial p_2} & 0 \\ 0 & 0 & 0 \end{bmatrix} \quad \boldsymbol{Q} = \begin{bmatrix} Q_1 \\ Q_2 \\ Q_t \end{bmatrix} = \begin{bmatrix} Q_{t1} + Q_{21} - Q_{12} - Q_{10} \\ Q_{t2} + Q_{12} - Q_{21} - Q_{20} \\ Q_{pump} - Q_{t1} - Q_{t2} \end{bmatrix}$$

Where Q_{ij} is mass flow from chamber i to j chamber , and the footmark '0' represents the atmosphere. V_i is further to be required for the solutions.

·Geometry of the Double Bellows

The geometry of the Double Bellows is shown in **Figure 2b** and **Figure S4**. We use a geometric average radius of the PVC tube to simplify calculations.

$$r = \sqrt{r_1 r_2}$$

The bending radius of chambers are

$$R_1 = R + sign\,(p_1 - p_2)\,s \tag{S13}$$

$$R_2 = R - sign\,(p_1 - p_2)\,s \tag{S14}$$

The axis lengths of chambers are

$$L_1 = [R + sign\,(p_1 - p_2)\,s]\,\theta \tag{S15}$$

$$L_2 = [R - sign\,(p_1 - p_2)\,s]\,\theta \tag{S16}$$

Since the steel wires constrain the central axis, the length L is constant.

$$L = R\theta \tag{S17}$$

Combining Equation (S13)-(S17), we can obtain the chamber volume.

$$V_1 = \frac{\theta}{2\pi} 2\pi^2 R_1 r^2 = \pi r^2 L \left[1 + sign\,(p_1 - p_2)\,\frac{s}{R} \right] \tag{S18}$$

$$V_2 = \frac{\theta}{2\pi} 2\pi^2 R_2 r^2 = \pi r^2 L \left[1 - sign\,(p_1 - p_2)\,\frac{s}{R} \right] \tag{S19}$$

Where the unknown R is to be solved by force equilibrium analysis.

The geometry variables and parameters are defined as follows.

θ-bending angle of the actuator
r-geometric average radius of the tube

13

r_1-internal radius of the tube
r_2-external radius of the tube
s-eccentricity of the chamber axis from the central axis
R-bending radius of the actuator
R_i-bending radius of chamber i
L-length of central axis
L_i-axis length of chamber i
V_i-instantaneous volume of chamber i

·*Force equilibrium of the Double Bellows*

Figure 2c *shows the section force diagram of the Double Bellows.*

The force caused by pressure is

$$F_{pi} = \pi r^2 p_i^{'}$$ (S20)

The elastic force from tube deformation is

$$F_i = F_i' + F_i'' = k(L_i - L)$$ (S21)

Where F_i' and F''_i are the equivalent component forces of F_i and the force couple M_i.

$$F_i' = \frac{1}{2}(F_i + kr\theta)$$ (S22)

$$F_i'' = \frac{1}{2}(F_i - kr\theta)$$ (S23)

$$M_i = (F_i' - F_i'')r$$ (S24)

The equilibrium Equation about axis-b is

$$-F_{p1}s + F_{p2}s + F_1 s - F_2 s + M_1 + M_2 = 0$$ (S25)

The mechanical variables are defined as follows.

k-*stiffness pf PVC tube*
p_i'-*gauge pressure of p_i*
F_{pi}-*pressure force*
F_i-*elastic deformation force*
F_i', F_i''-*equivalent conponent forces of F_i*

Combing Equation (S20)-(S25), we can obtain

$$R = \frac{2k(s^2 + r^2)L}{\pi r^2(p_1 - p_2)s}$$ (S26)

Substitute Equation (S26) into Equation (S18)-(S19).

$$V_1 = \pi r^2 L \left[1 + \frac{\pi r^2(p_1 - p_2)s^2}{2k(s^2 + r^2)L}\right]$$ (S27)

14

$$V_2 = \pi r^2 L \left[1 - \frac{\pi r^2 (p_1 - p_2) s^2}{2k (s^2 + r^2) L} \right] \tag{S28}$$

Supplementary Note 3. Modeling of the Triple Bellows

·Dynamic pressure of the Triple Bellows

*The air tank in the Triple Bellows (*i=1,2,3*) is also regarded as a chamber with a constant volume V_t . The chamber volume V_i is independent of V_t .*

$$V_i = f_i (p_1, p_2, p_3)$$

We specify Equation (1) on the Triple Bellows.

$$\dot{\boldsymbol{p}} = \begin{bmatrix} \dot{p}_1 \\ \dot{p}_2 \\ \dot{p}_3 \\ \dot{p}_t \end{bmatrix} \quad \boldsymbol{p} = \begin{bmatrix} p_1 \\ p_2 \\ p_3 \\ p_t \end{bmatrix} \quad \boldsymbol{V} = \begin{bmatrix} V_1 \\ V_2 \\ V_3 \\ V_t \end{bmatrix} \quad \frac{\partial \boldsymbol{V}}{\partial \boldsymbol{p}} = \begin{bmatrix} \frac{\partial f_1}{\partial p_1} & \frac{\partial f_1}{\partial p_2} & \frac{\partial f_1}{\partial p_3} & 0 \\ \frac{\partial f_2}{\partial p_1} & \frac{\partial f_2}{\partial p_2} & \frac{\partial f_2}{\partial p_3} & 0 \\ \frac{\partial f_3}{\partial p_1} & \frac{\partial f_3}{\partial p_2} & \frac{\partial f_3}{\partial p_3} & 0 \\ 0 & 0 & 0 & 0 \end{bmatrix} \quad \boldsymbol{Q} = \begin{bmatrix} Q_1 \\ Q_2 \\ Q_3 \\ Q_t \end{bmatrix} = \begin{bmatrix} Q_{t1} + Q_{21} + Q_{31} - Q_{12} - Q_{13} - Q_{10} \\ Q_{t2} + Q_{12} + Q_{32} - Q_{21} - Q_{23} - Q_{20} \\ Q_{t3} + Q_{13} + Q_{23} - Q_{31} - Q_{32} - Q_{30} \\ Q_{pump} - Q_{t1} - Q_{t2} - Q_{t3} \end{bmatrix}$$

Where Q_{ij} is mass flow from chamber i *to* j *chamber , and the footmark '0' represents the atmosphere. V_i is further to be required for the solutions.*

·Geometry of the Triple Bellows

The geometry of the Triple Bellows is shown in **Figure 3b** *and* **Figure S4**. *The geometric average radius of the PVC is the same as Equation (S12).*

$$r = \sqrt{r_1 r_2}$$

The Triple Bellows has two DOFs: bending relative to the ground and rotation above the z-axis. The rotation angle is

$$\varphi_i = \varphi + (i - 1) \frac{2}{3} \pi \tag{S29}$$

The bending radius of chamber i *is*

$$R_i = R - s_i \tag{S30}$$

Where

$$s_i = s \cos \varphi_i \tag{S31}$$

The axis length of chamber i *is*

$$L_i = R_i \theta \tag{S32}$$

Since the steel wires constrain the central axis, Equation (S17) is still satisfied.

$$L = R\theta$$

Combining Equation (S29)-(S32), we can obtain the chamber volume.

$$V_i = \frac{\theta}{2\pi} \cdot 2\pi^2 R_i r^2 = \pi\theta \left(R - s\cos\varphi_i\right) r^2 \tag{S33}$$

Where the unknown R and φ are to be solved by force equilibrium analysis.

The geometry variables and parameters are defined as follows.

φ-rotation angle above z-axis
φ_i-rotation angle of chamber i above z-zxis
s_i-projection length of s in bending direction

Those unmentioned parameters have the same definition as the Double Bellows.

·Force equilibrium of the Triple Bellows

Figure 3c *shows the section force diagram of the Triple Bellows.*

The force caused by pressure, the elastic force from tube deformation, the equivalent component forces of F_i and the equivalent force couple M_i follow the same law as Equation (S20)-(S24).

The equilibrium equations about axis-b and axis-r are

$$(F_{p1} - F_1)s_1 + (F_{p2} - F_2)s_2 + (F_{p3} - F_3)s_3 + M_1 + M_2 + M_3 = 0 \quad (F_{p1} - F_1)s\sin\varphi_1 + (F_{p2} - F_2)s\sin\varphi_2 + (F_{p3} - F_3)s\sin\varphi_3 = 0 \tag{S34}$$

Combing Equation (S20) -(S24) and Equation (S34), the numerical solutions of R and φ can be obtained.

Supplementary Note 4. Experimental tests of Double Bellows and Triple Bellows

·Experiments on Double Bellows

*The experimental parameters are set to be p_{low}=10 kPa, $p_{tank-low}$ = 120 kPa, and $p_{tank-high}$ =125 kPa. We use the experimental setup in **Figure S2a** to measure the actuator performance obeying the following procedures.*

i) Turn on the pump to pressurize the air tank (see Results-2.1. Working principle of the IEAR

mechanism)

*ii) For a specified p_{high} and Δp , actuate Double Bellows following the working flow chart **Figure 2d** for DIDO or **Figure 2e** for IEAR, whose timings of solenoid valves are presented in **Figure S2d**.*

iii) Wait for Double bellows to enter the steady-state pressure response.

iv) Record the actuation frequency f , air tank pressure p_{tank} , system power P , and the air temperature in the air tank by calculating their average on a window of 20 s.

v) Stop the actuation and exhaust the air in the actuator. For a new specified p_{high} and Δp , repeat step ii-v.

vi) Each specified working condition is measured seven times to reduce random error.

*In this work, the working pressure p_{high} with 50,60,70,80,90,100, and 75 kPa are covered, and the IEAR control parameter Δp=5, 10, and 15 kPa are measured (**Figure 2f-h**, **Figure S5a and b**, **Figure S6**). Based on the experiments, performance indicators are further calculated by the method in **Table 1** and **Supplementary Note 13**.*

*Notably, there is a deformation difference between DIDO and IEAR, as shown in **Figure 2d and e** (**Movie S3**). We may mention that these differences have limited influence on the comparison between DIDO and IEAR since the volume difference of PVC tube does not exceed **4.6%** even if the bending angle difference is up to 30deg (the difference in this work is markedly less than this value), which should not have a remarkable*

influence on the dynamic pressure governed by our model ($\dot{\boldsymbol{p}} = \xi \left[diag\left(\boldsymbol{V}\right) + diag\left(\boldsymbol{p}\right) \frac{\partial \boldsymbol{V}}{\partial \boldsymbol{p}} \right]^{-1} \boldsymbol{Q}$).

*Experiments on Triple Bellows

The experimental setup and parameters of Triple Bellows are the same as Doube Bellows with the following procedures.

i) Turn on the pump to pressurize the air tank (see Results-2.1. Working principle of the IEAR mechanism)

*ii) For a specified p_{high} and Δp , actuate Triple Bellows following the working flow chart **Figure 3d** for DIDO or **Figure 3e** for IEAR, whose timings of solenoid valves are presented in **Figure S2d**.*

iii) -vi) These steps are the same as Double Bellows.

*In this work, the working pressure p_{high} with 50,60,70,80,90,100, and 75 kPa are covered, and the IEAR control parameter Δp= 5, 10, and 15 kPa are measured (**Figure 3f-h**, **Figure S5c and d**, **Figure S7**). Based on the experiments, performance indicators are further calculated by the method in **Table 1** and **Supplementary Note 13**.*

Supplementary Note 5. Experiments on the robotic fin

*The structure of the robotic fin is presented in **Figure 4a and b**, whose materials and fabrication method are detailed in **Methods- 4.6. Materials and fabrication of the robots in applications**. We fixed the robotic fin on the end of a manipulator to stabilize the actuator during actuation (**Figure S8a**). The propulsion force is measured through a force sensor connected between the robotic fin and the manipulator. The experimental procedures are as follows.*

i) Move the manipulator downward to immerse the robotic fin in the water. The top of the robotic fin is about 5 mm below the water surface.

ii) Clear the force value.

*iii) Follow the same experimental steps i-v as testing Double Bellows (**Supplementary Note 4**). Notably, the real-time propulsion force is also recorded.*

iv) Move the manipulator upward and complete the experiments.

v) Each specified working condition is measured seven times to reduce random error.

For the experiments on the robotic fin, the working pressure p_{tank} with 50,60,70,80,90,100, and 75 kPa are covered, and is Δp set as a constant value of 10 kPa.

*Experimental results are shown in **Figure 4c-f**, the peak force is the maximum instantaneous propulsion force of the robotic fin, and the average force is a weighted average force in a flapping period of the robotic fin. According to the propulsion force formula $F = \rho u^2 s_a C_t$, a larger average force F can produce a larger average swimming velocity u.* [53]

17

Supplementary Note 6. Experiments on the fabric-based finger

*The structure of the robotic fin is presented in **Figure 4g** and **Figure S8d**, whose materials and fabrication methods are detailed in **Methods- 4.6. Materials and fabrication of the robots in applications.** The finger has a flexing and extending chamber, worn on a silicone hand with adult size through velcro. For the fabric-based finger, the experimental procedures are the same as testing Double Bellows (**Supplementary Note 4**), and the working pressure with p_{tank} 50,60,70,80,90,100 and 75 kPa are covered, and Δp is set as a constant value of 10 kPa. Also, each specified working condition is measured seven times to reduce random error.*

Supplementary Note 7. Extensive Experiments on the fiber-reinforced silicone actuator

*The fiber-reinforced silicone actuator has a symmetric structure with two chambers, and the fiber is coiled inside the silicone body during casting to prevent sliding (**Figure S9a**). All the experimental procedures and methods are the same as Double Bellows (**Supplementary Note 4**).*

Supplementary Note 8. Experiments on the quadruped robot

*The structure of the quadruped robot is presented in **Figure 5a-c** and **Figure S8g**, whose materials and fabrication method are detailed in **Methods- 4.6. Materials and fabrication of the robots in applications.** We set Δp =10 kPa, p_{low}=10 kPa, $p_{tank-low}$ = 120 kPa, and $p_{tabk-high}$ =125 kPa, the experimental procedures are as follows.*

i) For a specified p_{high} , put the quadruped robot at the starting line of the floorboard (with sandpaper preventing slipping).

*ii) Actuate the quadruped robot using the control method of Triple Bellows following the working flow chart **Figure 3d** for DIDO or **Figure 3e** for IEAR, whose timings of solenoid valves are presented in **Figure S2d**.*

iii) When the quadruped robot reaches the end line, stop actuation.

iv) Record the time consumed, steps to reach the ending line, air tank pressure , system power .

v) Repeat step i-v for a new specified p_{high} .

vi) Each specified working condition is measured seven times to reduce random error.

For the experiments on the quadruped robot, the working pressure p_{high} with 50,60,70,80,90,100 and 75 kPa are covered.

Supplementary Note 9. Comparative Experiments with EEAR

*A rigid air tank (100 mL) is introduced to the system as the air buffer to achieve EEAR (**Figure S9f** and **g**). Here, we should mention that a too-small air buffer may damage the air smoothness of the pipeline for this closed configuration, and on the other hand, a too-large air buffer may result in excessive pressure drop in the buffer during recirculation, reducing recycling capability.*

18

Based on the original system and the system with the air buffer introduced, we test the performance of four actuation modes: DIDO, IEAR, EEAR, and IEAR+EEAR. All the experiments follow the experimental procedures for Double Bellows and Triple Bellows.

Experimental results show the following findings in improving actuation speed and energy efficiency (**Figure S9h-k**).

  i) IEAR performs better than DIDO and EEAR.

  ii) EEAR hinders the improvement of actuation or efficiency within the range of low pressure,

  even worse than DIDO.

  iii) Actuation performance can benefit from the combination IEAR + EEAR. Especially for the

  range of high pressure, IEAR+EEAR achieves better performance than a single IEAR.

  iv) An adaptable best strategy is optional according to the results, which means adopting IEAR at low pressure and EEAR+IEAR at high pressure for robotic applications.

Supplementary Note 10. Characterization of pump flow Q_{pump}

We characterize the pump flow function by measuring the inflating process of an air tank, as is shown in **Figure S10a**. Since the air tank volume is constant, we can simplify the differential Equation (S7) as follows.

$$\dot{p}_t V_t = \xi Q_{pump} \tag{S35}$$

The time-based p_t is recorded in the experiments, and we have the pump flow function

$$Q_{pump}\left(p_t\right) = \frac{V_t}{\xi}\frac{dp_t}{dt} \tag{S36}$$

The air supply ability of the micro air pump decreases with the output pressure increasing.

Supplementary Note 11. Characterization of flow function

The mass flow Q_{ij} depends on the pressures on both sides of the air passage and the air passage itself, as is demonstrated in Equation (4).

$$Q_{ij} = \Psi_{ij}\left(p_i, p_j\right)\ \left(p_i \geqslant p_j\right)$$

Although empirical formulas [43,51,56–59] have approximated the flow function of an air passage conveniently, these models work well only when the pressure on one side remains constant. In our actuator, the pressures in both chambers change rapidly. It is more appropriate to obtain a data-driven flow function for greater accuracy.

We use two steel air tanks (10 L) to characterize the flow function of the air passage between a pair of chambers, as is shown in **Figure S10b**. The characterization has three steps: i) Pressurize air tank-1 to over 130 kPa. ii) Open the valve in the middle of the air passage and make the compressed air in tank-1 flow to tank-2. iii) When p_{high} decreases to have a difference of less than 2 kPa from p_{low}, close the valve. We try to keep downstream pressure p_{low} constant using a customized pneumatic testing system. To completely

characterize the mass flow under various working conditions, we repeat those steps under different p_{low} from 0 kPa to 120 kPa with a step length of 10 kPa. For those air passages deflating the compressed air into the ambient, tank-2 is removed during the test. The large 10 L air tanks reduce air pressure fluctuation and make the pressures change smoothly. All the data are recorded when the solenoid is fully open. We can obtain the experimental results as shown in **Figure S10c**.

$$\Psi_{ij}\left(p_{high}, p_{low}\right) = \frac{V_{high}}{\xi} \frac{dp_{high}}{dt} \tag{S37}$$

A quartic polynomial fits the experimental results to generate the data-driven flow function.

$$f\left(x, y\right) = a_{00} + \sum_{j=1}^{4} \sum_{i=1}^{j} a_{i,j-i} x^i y^{j-i} \tag{S38}$$

Supplementary Note 12. Correction of mass flow

$\Psi\left(p_{high}, p_{low}\right)$ is the mass flow when the valve is fully open. Actually, the response time (open/close time) cannot be ignored if the system generates high-frequency actions, especially when we employ cheap commercial solenoid valves. The actual mass flow should be corrected by a time-based open degree factor $\Gamma(t)$. According to Equation (5)

$$Q = \Gamma\left(t\right)\Psi\left(p_{high}, p_{low}\right), \Gamma \propto [0, 1]$$

$$\Gamma\left(t\right) = \frac{Q}{\Psi\left(p_{high}, p_{low}\right)} \tag{S39}$$

We use an air tank shown in **Figure S10d** to characterize the open degree of solenoid valves, which includes four steps: i) Inflate the air tank to 60 kPa (other air pressures are also feasible). ii) Open the valve and start recording the pressure in the tank simultaneously. iii) After an interval of $\Delta t(\Delta t \leq 1s)$, close the valve. iv) Continue recording pressure until $t = 1$ s.

As is shown in **Figure S10e**, both the opening and closing time between fully close and open states are about 0.2 s. The experimental results overall agree with the work of Xu et al. [65]. Notably, the response time of different valves varies due to inconsistent manufacturing quality. However, a more complicated situation is when the system generates high-frequency actions, the solenoid valve usually does not change between the fully close and open states. The state change may occur at any point between these two extreme states. We change Δt from 0.05 s to 0.25 s with an interval of 0.05 s, and the results are shown in **Figure S10f**. Here, we propose a time-based piecewise linear model to describe the open degree function.

***If the valve command changes from ON to OFF**

$$\Gamma\left(t\right) = \begin{cases} \Gamma_c & t - t_c < \left(1 - \Gamma_c\right)\tau_{ON} \\ \Gamma_c - \frac{t - t_c - \left(1 - \Gamma_c\right)\tau_{ON}}{\tau_{OFF}} & otherwise \end{cases}, \Gamma\left(t\right) \in [0, 1] \tag{S40}$$

·If the valve command changes from OFF to ON

$$\Gamma\left(t\right) = \begin{cases} \Gamma_c & t - t_c < \Gamma_c\tau_{OFF} \\ \Gamma_c + \frac{t - t_c - \Gamma_c\tau_{OFF}}{\tau_{ON}} & otherwise \end{cases}, \Gamma\left(t\right) \in [0, 1] \tag{S41}$$

20

Where t_c is the latest moment of command change, and Γ_c is the open degree at t_c .

Supplementary Note 13. Methods of statistics and error processing

*All the experimental indicators of actuation performance in **Table 1** are based on seven times measurements. The average and error are processed as the following methods.*

$$\bar{\hat{f}} = \frac{\sum \hat{f}_i}{n}$$

$$\hat{\sigma}_f = \sqrt{\frac{\sum \left(\bar{\hat{f}} - \hat{f}_i\right)^2}{n-1}}$$

$$\bar{\hat{p}}_{tank} = \frac{\sum \bar{\hat{p}}_{tank-i}}{n}$$

$$\hat{\sigma}_{P_{tank}} = \sqrt{\frac{\sum \left(\bar{\hat{p}}_{tank} - \hat{P}_{tank-i}\right)^2}{n-1}}$$

$$\bar{\hat{P}} = \bar{\hat{P}}_{allvalve} + \bar{\hat{P}}_{pump} = \frac{\sum \hat{P}_{allvalve-i}}{n} + \frac{\sum \hat{P}_{pump-i}}{n}$$

$$\hat{\sigma}_P = \sqrt{\hat{\sigma}^2_{P_{allvalve}} + \hat{\sigma}^2_{P_{pump}}} = \sqrt{\frac{\sum \left(\bar{\hat{P}}_{allvalve} - \hat{P}_{allvalve-i}\right)^2 + \sum \left(\bar{\hat{P}}_{pump} - \hat{P}_{pump-i}\right)^2}{n-1}}$$

$$\bar{e} = \frac{\bar{\hat{P}}}{\bar{\hat{f}}}$$

$$\hat{\sigma}_e = \sqrt{\left(\frac{1}{\bar{\hat{f}}}\hat{\sigma}_f\right)^2 + \left(\frac{\bar{\hat{P}}}{\bar{\hat{f}}^2}\hat{\sigma}_P\right)^2}$$

Supplementary Note 14. Comparative experiments with a large-scale air tank

A steel air cylinder (10 L) is serially connected between the pump and air tank (1L) to investigate the influence of a large air tank on the actuation performance. All other experimental configurations except the air cylinder are kept the same as Double Bellows.

*The experimental results in **Figure S9d** and **e** show that a large-scale air tank can decrease actuation speed and increase energy consumption per cycle, either for DIDO or IEAR. However, the influence is not remarkable based on existing experiments. This slight deterioration of actuation performance might be caused by the increase in air tank volume, which makes it more difficult for the pump to quickly pressurize the air tank and maintain the pressure $p_{tank-high}$ above the working pressure p_{high} under steady-state response.*

Supplementary Note 15. Design guidance on air supply strategies

For an air supply system, more channels require more components, such as pumps, valves, and air tanks, which has a remarkable influence on the size and portability of the system. We present a simple guidance on designing air supply systems with n channels (with simplification) as follows.

Table S2. Main components required by air supply strategies

	strategy	DIDO	EEAR	IEAR
	valves[1]	$2n^{(2)}$	$2n^{(3)}$	$C_n^2 + 2n^{(4)}$
c	air buffer	0	n	0
	pump	$\geq 1(most^5)$	$\geq 1(moderate)$	$\geq 1(least)$
	air tank	$\geq 0(most)$	$\geq 0(moderate)$	$\geq 0(least)$

1 The valves are two-position two-way valves, and the flow directivity is not considered in applications. (In this work, we consider the flow directivity for an accurate model, which doubles the required number of valves)
2 inlets for compressed air and outlets for exhaust air.

3 inlets for compressed air and outlets for exhaust air. Conservatively, we take one air buffer equivalent to two valves from the perspective of dimensions for the following analysis.
4 inlets for compressed air, outlets for exhaust air, and one-one connected valves.
5 These degree words describe the number of components required to achieve equivalent performance.

With the increase of n*, the size of the valve island increases due to more connections between chambers.*

N=1: DIDO and EEAR are optional for actuation

1<=N<5: The portability and actuation performance of IEAR are better than DIDO and EEAR

5<=N<6: Compared with DIDO, the complication of IEAR is larger than DIDO but with better performance. The portability and actuation performance of IEAR are better than EEAR.

N>=6: The complication of IEAR is larger than DIDO and EEAR but with better performance.

For N>=6, soft valves integrated into soft circuits can compose a compact valve island, which might further widen the application of IEAR under complicated conditions.